CHEMISTRY OF MATERIALS

pubs.acs.org/cm

Article

Charge Disproportionation and Complex Magnetism in a $PbMnO_3$ Perovskite Synthesized under High Pressure

Xiang Li, Zhiwei Hu, Yujin Cho, Xinyu Li, Hao Sun, Longzheng Cong, Hong-Ji Lin, Sheng-Chieh Liao, Chien-Te Chen, Anna Efimenko, Christoph J. Sahle, Youwen Long, Changqing Jin, Michael C. Downer, John B. Goodenough, and Jianshi Zhou*

Cite This: *Chem. Mater.* 2021, 33, 92−101

Read Online

ACCESS | Metrics & More | Article Recommendations

ABSTRACT: Because of the possible crossover of Pb and 3d transition-metal (T_M) redox levels, a charge transfer between Pb and T_M leads to a continuous evolution from $Pb^{2+}Ti^{4+}O_3$ to $Pb^{4+}Ni^{2+}O_3$ in the perovskite family of PbT_MO_3 as verified by several reports. However, very little information is known about $PbMnO_3$ in the PbT_MO_3 series. The perovskite $PbMnO_3$ is the most difficult one to synthesize, although its geometric tolerance factor is close to 1. Here, we report a careful study of $PbMnO_3$ synthesized under 15 GPa by a structural refinement and high-precision X-ray absorption spectroscopy (XAS) as well as a variety of measurements of physical properties. We can rationalize the physical properties of $PbMnO_3$ based on a local bonding model and the valence states of Pb and Mn from XAS. Moreover, the complete study of $PbMnO_3$ allows us to construct a more consistent picture of the valence evolution and the charge disproportionation for the entire family of PbT_MO_3 perovskites.

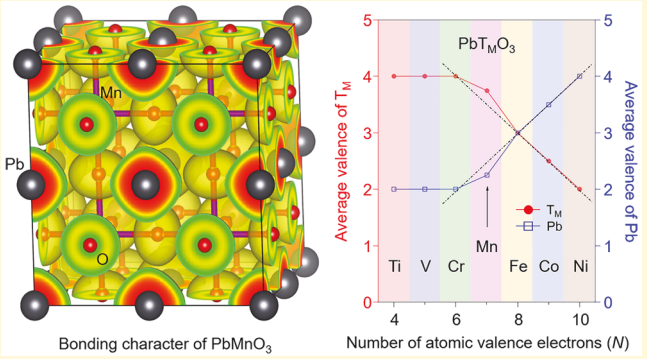

1. INTRODUCTION

Investigations of lead transition-metal perovskites PbT_MO_3 (T_M = 3d transition-metal) have highlighted the important role played by the valence state at the A-site Pb cations in determining the properties of these materials.[1−3] One striking observation is that the charge distribution between the A-site and B-site cations in PbT_MO_3 varies with the d^n manifolds of the transition metal due to the fact that the hybrid Pb 6s and 6p bands are close in energy to the O 2p bands and transition-metal d bands.[4] Across the 3d transition-metal row from left to right in the periodic table, $PbTiO_3$ with Ti^{4+} (d^0) and $PbVO_3$ with V^{4+} (d^1) exhibit the valence states of $Pb^{2+}T_M{}^{4+}O_3$,[5,6] whereas the oxidation state of $Pb^{4+}Ni^{2+}O_3$ with Ni^{2+} (d^8) has been determined.[7] The valence state crossover from Pb^{2+} to Pb^{4+} and from 4+ to 2+ for the transition metals between these two end members is not straightforward. The member of the family in which the charge disproportionation of Pb starts to occur is still unknown. The charge distribution of $PbCrO_3$ remains controversial. The charge disproportionation $3Cr^{4+} \rightarrow 2Cr^{3+} + Cr^{6+}$ has indicated a Pb^{2+} valence state in $Pb^{2+}Cr^{4+}O_3$ (Cr^{4+}: d^2).[8] Yu *et al.*, however, claimed a $Pb^{2+}{}_{0.5}Pb^{4+}{}_{0.5}Cr^{3+}O_3$ (Cr^{3+}: d^3) valence state based on structural and X-ray photoelectron spectroscopy measurements.[9] However, $PbFeO_3$ with Fe^{3+} (d^5) has been found to show a charge disproportionation of Pb^{3+} ions into Pb^{2+} and Pb^{4+} in $Pb^{2+}{}_{0.5}Pb^{4+}{}_{0.5}Fe^{3+}O_3$.[10] The Pb^{4+} concentration appears to increase as the atomic number Z of the transition metal further increases from Fe. The trend continues to T_M = Co and Ni. In $PbCoO_3$, however, in addition to the charge disproportionation of Pb, Co has been found to have a mixed valence state $Pb^{2+}{}_{0.25}Pb^{4+}{}_{0.75}Co^{2+}{}_{0.5}Co^{3+}{}_{0.5}O_3$ (Co^{3+}: d^6 and Co^{2+}: d^7).[4] Based on the data available to them, Sakai *et al.*[4] have proposed a crossover from Pb^{2+} to Pb^{4+} in the family of PbT_MO_3 perovskites. Perovskite $PbMnO_3$ has been synthesized at 15 GPa.[11] By using an iodometric-titration method, the authors gave a formula $Pb^{2+}Mn^{4+}O_3$ (Mn^{4+}: d^3), which clearly contradicts the formula $Pb^{2+}{}_{0.5}Pb^{4+}{}_{0.5}Mn^{3+}O_3$ predicted by Sakai *et al.*[4] The primary goal for this work is to determine the charge distribution in $PbMnO_3$ by X-ray absorption spectroscopy (XAS).

For the perovskite structure, the geometric tolerance factor t defined as $t \equiv (Pb{-}O)/\sqrt{2}(T_M{-}O)$, where $(Pb{-}O)$ and $(T_M{-}O)$ are equilibrium bond lengths, provides a measure-

Received: June 26, 2020
Revised: November 11, 2020
Published: November 24, 2020

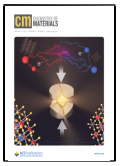

https://dx.doi.org/10.1021/acs.chemmater.0c02706
Chem. Mater. 2021, 33, 92−101

ment of the structural stability. A cubic structure is found for $t = 1$; For $t < 1$, the bond length mismatch is accommodated by cooperative octahedral-site rotations that result in bending the T_M-O-T_M bond from 180°; for $t > 1$, the oxide either undergoes a ferroelectric displacement like in $PbTiO_3$[12] and $PbVO_3$[5] or adopts a polytype structure.[13] An earlier study has shown that an oxygen-stoichiometric hexagonal-perovskite polytype (6H) of $PbMnO_3$ can be stabilized under 8 GPa at 1073 K owing to a $t > 1$. The valence state of 6H−$PbMnO_3$ has been confirmed to be $Pb^{2+}Mn^{4+}O_3$ by iodometric titration and the unit-cell composition calculated from its structural model.[11,14] Generally speaking, the Pb−O bond is more compressible than the T_M-O bond, which makes factor t decrease under high pressure. The high-pressure phases with a reduced t factor can normally be quenched to ambient conditions as has been found in cubic $BaRuO_3$.[15] Therefore, a cubic $PbMnO_3$ is expected if it is made under a sufficiently high pressure. Surprisingly, a tetragonal phase of $PbMnO_{2.94}$ with a small tetragonal distortion ($c/a = 1.017$) is stabilized under 15 GPa at 1273 K, which is similar to that found in $BaIrO_3$.[16] The origin of this structural distortion is still unclear. Furthermore, similar to $PbTiO_3$ and $PbVO_3$, a ferroelectric perovskite $PbMnO_3$ is expected for a t slightly larger than 1. A recent first-principles density functional theory (DFT) calculation indeed predicted that the polar $P4mm$ phase has a ground-state energy slightly lower than that of the nonpolar $P4/mmm$ phase.[17] However, a structural analysis based on a synchrotron X-ray diffraction pattern suggests that the tetragonal phase of $PbMnO_3$ adopts a nonpolar structure with the space group of $P4/mmm$.[11] To date, the available data on $PbMnO_3$ are insufficient to distinguish whether it adopts the polar structure $P4mm$ seen in $PbTiO_3$ and $PbVO_3$ or the nonpolar structure $P4/mmm$. It is useful to compare $PbMnO_3$ with other perovskite oxides with Mn^{4+} like $SrMnO_3$.[18] Although the size of the Pb^{2+} ion (1.49 Å) is comparable to that of the Sr^{2+} ion (1.44 Å), the perovskite $PbMnO_3$ has been reported to show an antiferromagnetic (AFM) order with a Néel temperature $T_N = 20$ K,[11] which is much lower than $T_N = 233$ K of $SrMnO_3$.[18] Oka *et al.* have argued that a double-exchange ferromagnetic (FM) interaction resulting from e_g electrons hopping between Mn^{3+} and Mn^{4+} neighbors weakens the AFM super-exchange interactions through the $t_2^3-O-t_2^3$,[11] so as to lower T_N. Alternatively, a more covalent bonding of the π-bonding Pb−O bond than that of the Sr−O bond clearly plays an important role in suppressing the magnetic transition temperature as seen in $Pb_{1-x}Sr_xRuO_3$.[19] In order to understand these unusual structural and physical properties in the perovskite $PbMnO_3$, we have determined the valance states of Pb and Mn by using XAS at the Pb-L_3 and Mn-$L_{2,3}$ edges, respectively, and measured transport and magnetic properties.

2. EXPERIMENTAL SECTION

A polycrystalline sample of tetragonal $PbMnO_3$ was synthesized under 15 GPa and 1473 K in a Walker-type multi-anvil module (Rockland Research Co.). The mixed powder of PbO_2, MnO_2, and $KClO_4$ (Alfa, 99.9%+) with a molar ratio of 1:1:1 as starting materials was pressed into a small pellet and sealed in a platinum crucible. A crucible was inserted into a BN sleeve and then placed at the center of a Mo heater with two $LaCrO_3$ plugs at the ends. A cylindrical $LaCrO_3$ sleeve was used to ensure better thermal isolation and a Cr-doped MgO octahedron with 12 mm edge length was used as a pressure medium. A single-phase sample was obtained only if the crucible was sealed well and the sintering temperature was above 1473 K.

High-resolution synchrotron X-ray powder diffraction (SXRPD) data at room temperature (RT) were collected at beamline 11-BM at the Advanced Photon Source (APS), Argonne National Laboratory with a wavelength of 0.45789 Å. Rietveld refinement of the SXRPD pattern was done with software Fullprof.[20] Second harmonic generation (SHG) microscopy was measured with a Ti/sapphire laser operating at 780 nm wavelength (76 MHz repetition rate, 150 fs pulse width). The *p*-polarized laser was incident on the sample at an angle of 45° and the signal was detected by a photo-multiplier tube. Soft XAS spectra at the Mn-$L_{2,3}$ edges were measured at the 11 A beamline of NSRRC Taiwan by using a total electron yield method; the high-resolution partial fluorescence yield (PFY) Pb-L_3 XAS spectra with an overall resolution of ~1.0 eV was measured at the ID 20 beamline of the ESRF, France.[21] The emission energy of the spectrometer was tuned to the peak of the Pb-$L_{\alpha 1}$ emission line and the incident photon energy was scanned through the Pb-L_3 edge. The Pb-L_3 spectra of $PbMnO_3$ and the Pb^{4+} reference in $PbNiO_3$ were normalized at 95 eV above the absorption edge. Thermogravimetric analysis (TGA) was conducted on a Setaram TG-DTA device at a heating rate of 5 K/min up to 1200 K in a mixture of hydrogen (10%) and argon (90%) gases. Resistivity and specific heat were measured with a physical property measurement system (PPMS) from Quantum Design. Thermoelectric power was measured with a homemade apparatus. Magnetization was measured with a vibrating sample magnetometer (VSM) on the PPMS.

DFT calculations were performed with the projector augmented wave method[22,23] as implemented in the Vienna *Ab initio* simulation package.[24,25] Spin-polarized calculations were conducted based on a supercell containing 40 atoms. A PBEsol + U functional was applied to the d^n manifold of Mn with $U = 6.9$ eV and $J_H = 1$ eV. A 5 × 5 × 5 *k*-points mesh, a plane-wave cutoff of 600 eV, and a force convergence tolerance of 2.5 meV/Å were employed in the structural relaxation. The density of states and band structure were calculated by using the code HSE06.[26]

3. RESULTS

3.1. Structural Characterizations. Figure 1 shows the Rietveld analysis result of the SXRPD pattern at RT. We find

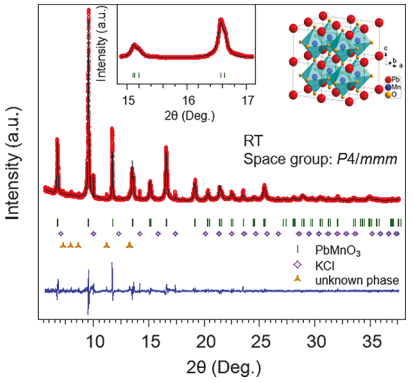

Figure 1. SXRPD pattern of tetragonal perovskite $PbMnO_3$ at RT with the space group $P4/mmm$ (no. 123). The inset of the left panel shows the profile at 2θ angles between 15 and 17°. The inset of the right panel shows the crystal structure of $PbMnO_3$.

that the major phase of $PbMnO_3$ (vol. ~96%) has a tetragonal structure with a space group $P4/mmm$ (no. 123) that is consistent with a previous work.[11] Refinements with the lattice parameters of $a = 3.8975(1)$ Å and $c = 3.8654(1)$ Å give a good profile fitting of diffraction peaks, as illustrated in the inset of left panel in Figure 1, which indicates a small tetragonal distortion ($c/a = 0.992$). A small amount of impurities (vol. ~4%), including KCl and an unknown phase, is present in the sample. The high-resolution SXRPD enables

https://dx.doi.org/10.1021/acs.chemmater.0c02706
Chem. Mater. 2021, 33, 92−101

us to determine the atomic displacement parameters (ADPs) of heavy atoms and structural disorder. Table 1 summarizes the

Table 1. Structural Refinement of $PbMnO_3$ with the Space Group *P4/mmm* (No. 123)[a] at RT

atom	*x*	*y*	*z*	B_{iso}/Å^2	Occ
O1 (1c)	0.5	0.5	0	0.80	1.00
O2 (2e)	0.5	0.0	0.5	0.80	2.00
Pb (1a)	0	0	0	1.51(1)	1.00
Mn (1d)	0.5	0.5	0.5	0.98(1)	1.00

[a]The lattice parameters: a = 3.8975(1) Å, c = 3.8654(1) Å, and V = 58.717 (1) Å^3 and R_p = 8.64, R_{exp} = 8.43, and χ^2 = 1.90.

refined lattice parameters, atomic positions, ADPs (B_{iso}), and occupancy factors (Occ). A large B_{iso}(Pb) of 1.51(1) Å^2 at the Pb site and a B_{iso}(Mn) of 0.98(1) Å^2 at the Mn site reveal large positional disorders in $PbMnO_3$. It should be noted that similar reliability R values were obtained by fitting the SXRPD profile with either a nonpolar *P4/mmm* or polar *P4mm* symmetry. Because it is difficult to determine precisely the oxygen positions by X-ray if it adopts the polar structure, we are not able to distinguish the polar *versus* nonpolar structural models used to refine the SXRPD pattern. Alternatively, the highly sensitive optical SHG has a noteworthy advantage in probing a polar structure.

Figure 2 displays a side-by-side comparison of the SHG mapping on the polished sample surface between $PbMnO_3$ and

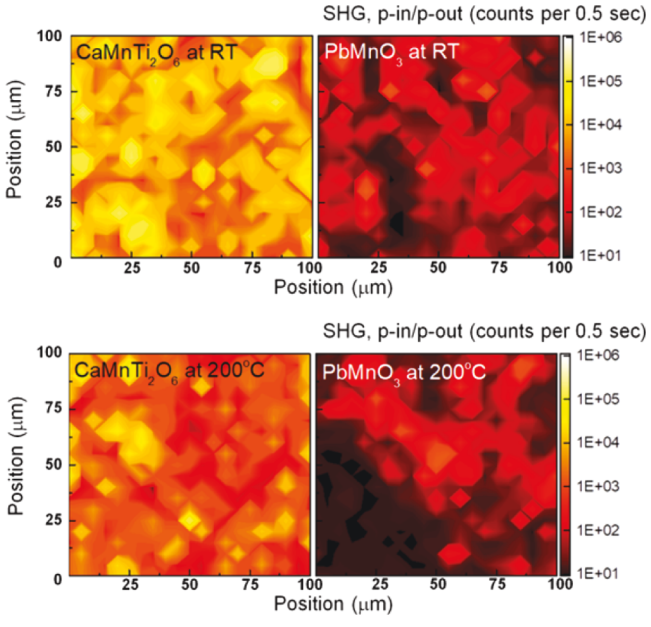

Figure 2. SHG micrographs on $PbMnO_3$ and $CaMnTi_2O_6$: top panels were measured at RT and the bottom panels were measured at 200 °C. The average SHG of $PbMnO_3$ was extremely weak and nearly temperature independent.

a polar oxide $CaMnTi_2O_6$. $CaMnTi_2O_6$ is a ferroelectric[27] showing a strong and pronounced temperature-dependent SHG signal. In contrast, the SHG response from $PbMnO_3$ is nearly temperature independent and much weaker, by at least two orders of magnitude than that from $CaMnTi_2O_6$, which can be attributed to a symmetry-breaking on the sample surface. These observations provide convincing evidence that $PbMnO_3$ adopts the nonpolar *P4/mmm* symmetry rather than the predicted polar *P4mm* structure at least above RT. Based on the nonpolar structural model, the Pb atoms are not allowed to displace from the 1*a* position (0, 0, 0). Therefore, the tetragonal distortion (c/a = 0.992) does not have the same origin as that in $PbTiO_3$ and $PbVO_3$ and needs to be further scrutinized together with the results of other physical properties.

3.2. Charge Distribution from XAS. We now turn to the determination of the valence states of the Mn and Pb ions in $PbMnO_3$ by XAS spectra. The soft XAS spectra at the 3d transition-metal $L_{2,3}$ edges are highly sensitive to the valence state; an increase of the valence state causes a shift of the XAS-$L_{2,3}$ spectrum toward higher energies.[28,29] Figure 3a shows the

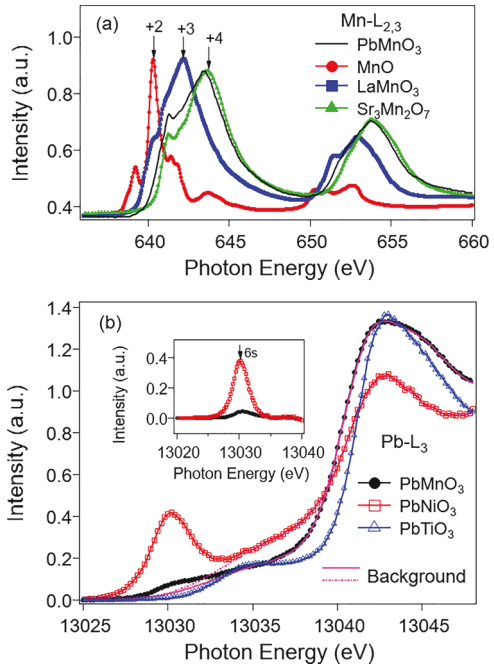

Figure 3. (a) Mn-$L_{2,3}$ XAS of $PbMnO_3$ compared to that of MnO (Mn^{2+}), $LaMnO_3$ (Mn^{3+}), and $Sr_3Mn_2O_7$ (Mn^{4+}), respectively and (b) PFY Pb-L_3 XAS of $PbMnO_3$ together with those of $PbNiO_3$ (Pb^{4+}) and $PbTiO_3$ (Pb^{2+}). The inset: the spectral integral area of I_{6s} after subtracting the background.

Mn-$L_{2,3}$ XAS spectra of $PbMnO_3$ together with those of MnO, $LaMnO_3$, and $Sr_3Mn_2O_7$ for comparison. It has been shown that the valence states of Mn ions in the reference compounds of MnO, $LaMnO_3$, and $Sr_3Mn_2O_7$ are +2, +3, and +4, respectively; the peak positions of $PbMnO_3$ at the Mn-$L_{2,3}$ edges are located between those of Mn^{3+} and Mn^{4+} but are closer to Mn^{4+}. The average valence state of Mn ions in $PbMnO_3$ can be estimated to be +3.75, according to the relative energy shift of the absorption edge.

Figure 3b presents the Pb-L_3 XAS spectrum of $PbMnO_3$ together with those of $PbTiO_3$ and $PbNiO_3$ used as the reference of Pb^{2+} and Pb^{4+}, respectively. Unlike the XAS spectra of the transition metal at L and K edges, where the energy positions of the strong white line and absorption edge are very sensitive to the number of localized d valence electrons, at the Pb-L edge, there is no clear white line and the energy position is strongly affected by the crystal structure, so it is less sensitive to the Pb valence state. Fortunately, the Pb-L_3 XAS spectra taken from the high-resolution PFY mode provide an opportunity to identify the valence state of Pb. As

https://dx.doi.org/10.1021/acs.chemmater.0c02706
Chem. Mater. 2021, 33, 92−101

shown in Figure 3b, one finds a sharp lower energy shoulder I_{6s} at 13,030 eV in the PFY spectrum that cannot be observed in normal transmission spectra.[3] This lower energy pre-edge peak can be assigned to the dipole allowed transition from the $2p_{3/2}$ core level to the unoccupied 6s states, while the main peak at 13,040 eV can be assigned to the transitions from the $2p_{3/2}$ core level to the empty Pb 6d states.[3,30] The pre-edge peak I_{6s} can be observed for the Pb^{4+} ion with two 6s holes, but it is absent for the Pb^{2+} ion with a fully occupied 6s state. Thus, the spectral intensity of the pre-edge peak I_{6s} can be used to determine the valence change of Pb. To calculate the spectral intensity, the broad background between 13,020 and 13,040 eV has been described by an analytic function related to electron states and edge jump,[3,31] which can be simulated with a superposition of an arctan-like function and Gaussian lines, as shown in Figure 3b (pink curves). After subtracting the background, the spectral integral area of I_{6s} is presented in the inset of Figure 3b. The intensity ratio of I_{6s} between $PbMnO_3$ and $PbNiO_3$ is about 1/8, which indicates that the average valence state of the Pb ions in $PbMnO_3$ is +2.25. Moreover, a total weight loss of 10.44% observed by TGA, as shown in Figure 4, from the as-made sample to Pb metal and MnO

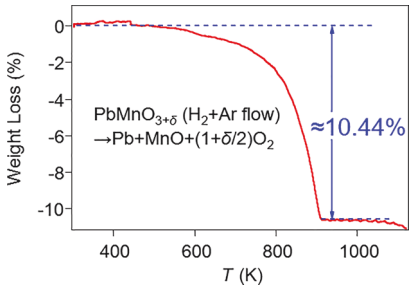

Figure 4. Thermogravimetric data for the decomposition of $PbMnO_3$ on heating from RT to 1200 K in a gas flow of hydrogen (10%) and argon (90%).

identified by XRD indicates that the as-made sample is nearly oxygen stoichiometric (3 ± 0.03); this result is consistent with the previous report of iodometric titration.[11] Because Pb prefers the valence states of Pb^{2+} and Pb^{4+},[32] the charge distribution of the as-made $PbMnO_3$ can be assigned as $Pb^{2+}_{0.875}Pb^{4+}_{0.125}Mn^{3+}_{0.25}Mn^{4+}_{0.75}O_3$ based on the valance state of Pb and Mn ions.

3.3. Transport Properties. The temperature dependence of resistivity $\rho(T)$ under different magnetic fields and zero-field thermoelectric power $S(T)$ of $PbMnO_3$ are shown in Figure 5a,b, respectively. Reliable data of $\rho(T)$ can be only obtained at $T > 150$ K because the extremely high resistance of the sample is comparable to that of the input resistance of the voltmeter used in the measurements at low temperatures; $S(T)$ also becomes noisy for $T < 150$ K. The zero-field resistivity increases dramatically with decreasing temperature, thereby indicating an insulating behavior for the temperature range we examined; no obvious magnetoresistance effect has been observed in an applied field up to 9 T. The inset of Figure 5a presents the plot of zero-field lnρ *versus* inverse temperature T^{-1}, which can be well fitted to the activation transport formula of $\rho \propto \exp(E_\rho/k_BT)$, where k_B is the Boltzmann's constant and the thermal activation energy E_ρ is 0.19 eV. This observation is opposite to the result of recent theoretical calculation[17] and to the calculated result presented in this work that gives metallic $PbMnO_3$. On the other hand, Figure 5b

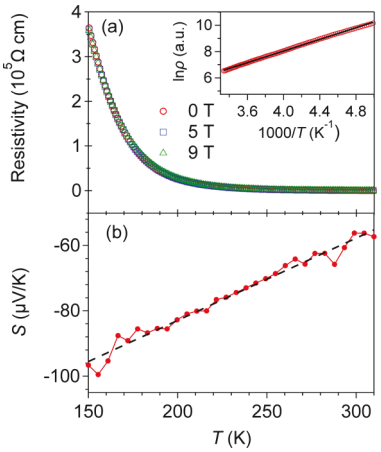

Figure 5. Temperature dependence of (a) resistivity $\rho(T)$ and (b) thermoelectric power $S(T)$ of $PbMnO_3$.

shows that the magnitude of the thermoelectric power S at RT is smaller than that found in most insulators. In this perovskite with mixed valence $Mn^{3/4+}$, carriers are progressively trapped as the sample is cooled down from RT as indicated by an enlarged magnitude of $S(T)$ at low temperatures. The negative $S(T)$ is an indicator of an *n*-type semiconductor.

3.4. Magnetic Properties and Specific Heat. Figure 6a shows the magnetization as a function of temperature

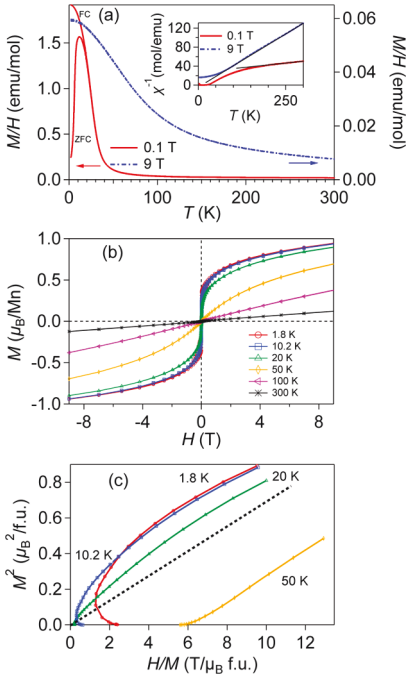

Figure 6. (a) Temperature dependence of magnetization under 0.1 and 9 T from 1.8 to 300 K; (b) field dependence of magnetization over the range -9 T $\leq H \leq 9$ T; and (c) Arrott plot of $PbMnO_3$ at different temperatures.

measured with fields of 0.1 and 9 T in the warming run after zero-field cooling (ZFC) and field cooling (FC). The data with $H = 0.1$ T are qualitatively similar to those obtained by Oka *et al.*, that is, the ZFC and FC curves diverge around 20 K,[11] whereas $\chi(T)$ shows a FM transition at $T_c \sim 20$ K(more obvious in the inset), a clear splitting between the ZFC and FC curves is indicative of an AFM spin structure. Additionally, the

https://dx.doi.org/10.1021/acs.chemmater.0c02706
Chem. Mater. 2021, 33, 92−101

inverse magnetic susceptibility $\chi^{-1}(T)$ is not linear at $T > T_c$. The part of $\chi^{-1}(T)$ at 0.1 T for $T > 150$ K can be fit to the Curie–Weiss (CW) law with a Weiss constant $\theta_{CW} = -266$ K and an effective moment $\mu_{eff} = 9.4\ \mu_B$. The linear part of $\chi^{-1}(T)$ at 9 T extends to ~70 K and fitting to the CW law gives a $\mu_{eff} = 4.3\ \mu_B$ with $\theta_{CW} = 5.4$ K. The sharply different fitting results suggest a possible field-induced transition from an AFM phase to a FM phase. We will return to this point in the Discussion section. The obtained μ_{eff} from the $\chi^{-1}(T)$ at 9 T is close to the spin-only value of 4.2 μ_B based on the formula of $Pb^{2+}_{0.875}Pb^{4+}_{0.125}Mn^{3+}_{0.25}Mn^{4+}_{0.75}O_3$.

Figure 6b displays the field dependence of magnetization at different temperatures. At $T = 1.8$ K, the saturation magnetization M_{sat} at 9 T approaches ~0.94 μ_B/Mn. Moreover, nonlinear $M(H)$ curves can be found for temperatures up to 50 K, revealing that a spin ordering emerges below this temperature. Nearly parallel lines at high fields in the Arrott plot M^2 *versus* H/M, as shown in Figure 6c, indicate that $PbMnO_3$ is a ferromagnet described by the mean field theory for itinerant electron ferromagnetism. An isotherm passing through the origin can be derived from the Arrott plot at a temperature around 20 K, which is the critical temperature of FM spin ordering.

Specific heat data reveal useful information about magnetic ordering. Figure 7a shows the specific heat $C(T)$ of $PbMnO_3$ measured in the temperature range from 1.8 to 300 K. At low temperatures, the specific heat $C(T)$ can be well described by the formula $C/T = \gamma + \beta T^2$, as shown in the inset of Figure 7a, yielding coefficients of electron contribution $\gamma = 27.3(6)$ mJ/mol K^2 and lattice contribution $\beta = 1.04(1)$ mJ/mol K^4. A relatively high γ can be related to free electrons at the Fermi energy. Then, the activated behavior in the $\rho(T)$ of Figure 5a can be attributed to grain boundary scattering. The Debye temperature θ_D can be derived as 210(1) K. In contrast to the magnetic ordering from the magnetization measurement, a brief overview of the $C(T)$ does not show an obvious signature of a magnetic ordering. After subtracting $C_{lattice}$, which is obtained by fitting the $C(T)$ in the temperature range 1.8–300 K to the Debye–Einstein model (see Figure 7b up to 50 K), we are able to extract the magnetic contribution $C_{mag} = C_{total} - C_{lattice}$. As can be seen in Figure 7c, C_{mag} has a broad hump in the temperature range between 10 and 30 K instead of a typical λ-shape profile. Nevertheless, it corresponds well to the anomaly of magnetic susceptibility. The entropy on crossing the transition in Figure 7c is helpful for estimating the degree of spin ordering on crossing the transition. The obtained entropy change $\Delta S \approx 0.2$ J/mol K is much smaller than the expected value 11.5 J/mol K for a localized $S = 3/2$ system of Mn^{4+} (t_2^3), which indicates that a small number of spins are involved in the transition in the zero field.

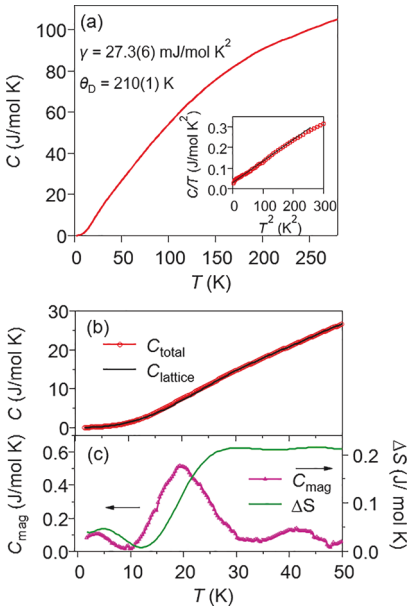

Figure 7. Temperature dependence of (a) specific heat $C(T)$ at the zero field from 1.8 to 300 K; (b) lattice contribution $C_{lattice}$ (T) obtained by fitting the Debye–Einstein model to $C(T)$; and (c) magnetic specific heat C_{mag} (T) and magnetic entropy change ΔS at low temperatures of $PbMnO_3$.

3.5. Calculated Electronic Structure. The band structure and the electron density of states (DOS) are shown in Figure 8a–c, respectively. Several dispersion curves cross the Fermi energy E_F, most of the curves form narrow bands. The major contributions of DOS at E_F come from the O 2p band and Pb 6s band. The prediction of metallic $PbMnO_3$ is consistent with a finite γ from the specific heat measurement. A clear exchange splitting is consistent with the magnetic transition. The calculated result of the ground-state energy with different types of magnetic ordering is given in Table 2. A FM phase has the lowest energy, this conclusion also is consistent with the

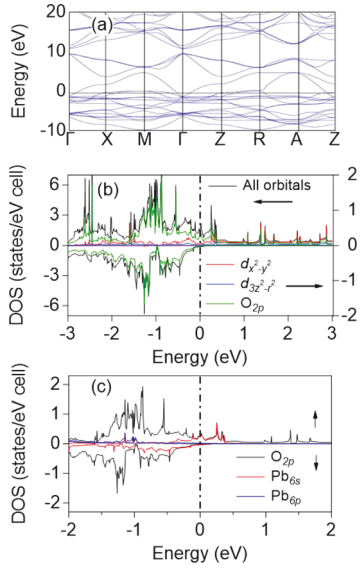

Figure 8. (a) Band structure and (b,c) DOS projected on the Pb, Mn, and O atomic orbitals in the tetragonal perovskite phase of $PbMnO_3$; the arrows ↑ and ↓ indicate spin-up and spin-down, respectively.

Table 2. System Energy of $PbMnO_3$ with Different Types of Magnetic Ordering by the DFT Calculation

	lattice constant (Å)	octahedral volume (Å^3)	Mn–O_{xy} distance (Å)	energy (eV)
A-type AFM	3.8762	9.4737	1.9226	0.0607
C-type AFM	3.7983	9.4543	1.9214	0.0632
G-type AFM	3.8271	9.3443	1.9137	0.1814
FM	3.8518	9.5266	1.9260	0.0000

https://dx.doi.org/10.1021/acs.chemmater.0c02706
Chem. Mater. 2021, 33, 92–101

analysis of $\chi(T)$ at high magnetic fields. By relaxing the crystal structure, the most stable crystal structure from the calculation is not the tetragonal phase but a simple cubic perovskite structure. A much enhanced $\gamma = 27.3$ mJ/mol K^2 relative to the calculated $\gamma_0 = 3.5$ mJ/mol K^2 suggests that electrons in $PbMnO_3$ are strongly correlated. Despite the great success of the structure and property predictions by a first-principles calculation for a broad range of materials, the augmented plane wave (APW) appears to be too far from the real electron distribution for the Pb lone-pair electrons, especially the hybridization with the narrow bands of Mn 3d and O 2p, which may be the origin of the tetragonal distortion found in $PbMnO_3$. Nevertheless, our calculation successfully predicts nonpolar $PbMnO_3$. By using an electron localization function (ELF),[33] we have analyzed the bonding character of $PbMnO_3$ and compared with that of $PbVO_3$, as shown in Figure 9. Our

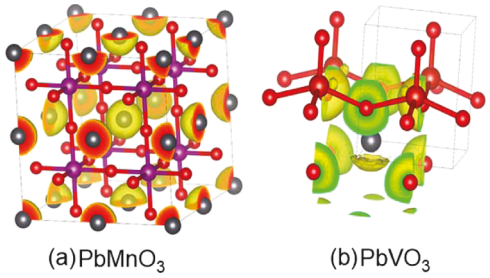

Figure 9. Valance electrons ELF isosurface around (a) Pb in $PbMnO_3$ and (b) Pb and O in $PbVO_3$.

calculated result for $PbVO_3$ is identical to that in the literature, the lone-pair $6s^2$ electrons form a hat-like cloud on one side of the Pb^{2+} ions along the c axis. The more covalent bonding between the lone-pair electrons and O 2p pulls the apical oxygen from the middle between VO_2 planes, which appears to be the driving force for the formation of the polar structure. In contrast, the localized 6s electrons are distributed uniformly around Pb in $PbMnO_3$.

4. DISCUSSION

4.1. Crystal Structure. The *P*4/*mmm* structure resolved from the refinement of the SXRPD pattern is unusual for a perovskite oxide with t slightly larger than 1, which normally leads to hexagonal polytypes or a polar structure for oxides made under ambient pressure.[13] The t factor in ABO_3 oxides reduces under high pressure, so that a $t = 1$ for the cubic phase can be reached under high pressure. Therefore, the high-pressure and high-temperature phase quenched to ambient conditions should have the B−O bond under tension, which normally gives rise to a cubic phase. The *P*4/*mmm* structure gives no tilting of the octahedra, but it allows an elongated octahedron along the a axis. The averaged Mn−O bond length, 1.944 Å, is significantly larger than 1.903 Å extracted from the cubic $SrMnO_3$ with Mn^{4+}.[18] In comparison, the Jahn−Teller (JT) active Mn^{3+} in $LaMnO_3$ has an averaged Mn−O bond length 2.020 Å.[34] In the ionic model, we can use the bond valance sum (BVS) to calculate the actual valance of cations.[35] Based on the bond lengths from the structural study, we obtained the BVS = 3.6, which is close to the XAS result.

In order to understand better the structure of $PbMnO_3$ and the evolution of chemical and physical properties in the PbT_MO_3 perovskites, it will be useful to start the discussion from the tolerance factor t. Table 3 lists the t values and other

Table 3. Structural Parameters and Physical Properties of PbT_MO_3 Perovskites

compound	$PbTiO_3$[37]	$PbVO_3$[38]	$PbCrO_3$[39]	$PbMnO_3$	$PbFeO_3$[10]	$PbCoO_3$[4]	$PbNiO_3$[7]
space group	*P*4*mm*	*P*4*mm*	$Pm\bar{3}m$	*P*4/*mmm*	unknown	$Pn\bar{3}$	*Pnma*
T	1.02	1.04	1.02	1.01	0.93	0.91	0.83
GII	0.139	0.249	0.156	0.451	0.279	0.424	0.059
valence distribution	$Pb^{2+}Ti^{4+}O_3$	$Pb^{2+}V^{4+}O_3$	$Pb^{2+}Cr^{4+}O_3$	$Pb^{2+}_{0.875}Pb^{4+}_{0.125}Mn^{3+}_{0.25}Mn^{4+}_{0.75}O_3$	$Pb^{2+}_{0.5}Pb^{4+}_{0.5}Fe^{3+}O_3$	$Pb^{2+}_{0.25}Pb^{4+}_{0.75}Co^{2+}_{0.5}Co^{3+}_{0.5}O_3$	$Pb^{4+}Ni^{2+}O_3$
applied pressure for synthesis	ambient pressure	6 GPa	5 GPa	15 GPa	7 GPa	12 GPa	3 GPa
physical properties	ferroelectric insulator	AFM insulator	AFM insulator	FM metal	unknown	AFM insulator	AFM insulator
	$T_c = 764$ K	$T_N = 180$ K	$T_N = 245$ K	$T_c \sim 20$ K		$T_N = 8$ K	$T_N = 225$ K

https://dx.doi.org/10.1021/acs.chemmater.0c02706
Chem. Mater. 2021, 33, 92−101

structural parameters of the PbT_MO_3 series. On the side $t > 1$, $PbTiO_3$ and $PbVO_3$ favor the tetragonal structure of *P4mm* and are ferroelectric. On the side $t < 1$, both $PbFeO_3$ and $PbCoO_3$ show cooperative octahedral-site rotations in their structures. Accordingly, the reduction of t values agrees well with the increasing ratio of the smaller Pb^{4+} ions. It is important to know that the tetragonal $PbMnO_3$ with $t = 1.01$ is located at the boundary between the polar structure with displacive Pb ions ($t > 1$) and the distorted structure with a cooperative rotation of the MnO_6 octahedra ($t < 1$). The consideration based on the t factor alone fails to predict the tetragonal phase found in the experiment. The driving forces for the structural distortion may include the bonding mismatch because of the interaction between the Pb-sp hybrid and Mn-e_g orbitals. In addition to the t factor, whether a particular crystal structure for a given chemical formula can be stabilized easily depends on the global instability index (GII), which can be calculated for the perovskite structure with software of SPuDS.[36] In comparison with GII = 0.005, for a simple perovskite $SrTiO_3$, a much larger GII = 0.451 is obtained for $PbMnO_3$ with the tetragonal structure *P4/mmm*. A compound with a large GII is unstable and can normally be made only through a special synthesis route, such as a high-pressure synthesis. GII values calculated for all PbT_MO_3 are listed in Table 3, which is generally consistent with the argument that the synthesis of a perovskite with a high GII must be made under higher pressure.

4.2. Evolution of the Valance State in PbT_MO_3. Our XAS result shows that $PbMnO_3$ has a $Pb^{2+}_{0.875}Pb^{4+}_{0.125}Mn^{3+}_{0.25}Mn^{4+}_{0.75}O_3$ valence state, which clearly deviates from the interpretation in the paper by Sakai *et al.* that the valence distribution of $PbMnO_3$ is $Pb^{2+}_{0.5}Pb^{4+}_{0.5}Mn^{3+}O_3$ estimated from the two neighboring perovskite $PbCrO_3$ and $PbFeO_3$.[4] The updated picture of the valence change in PbT_MO_3 is illustrated in Figure 10a; T_M^{4+} holds for $PbTiO_3$, $PbVO_3$, and $PbCrO_3$, which is followed by a linear decrease of valence on T_M from +4 in $PbCrO_3$ to +2 in $PbNiO_3$, except for a clear deviation observed for $PbMnO_3$. Corresponding to the decrease of the valence on T_M, the valance on Pb increases linearly. Such a valence evolution can be attributed to the fact that the d-orbital redox potentials move to lower energy relative to the $Pb^{2+/3+}$ redox level as the valence electron number N increases in the 3d transition metal (see Figure 10b).

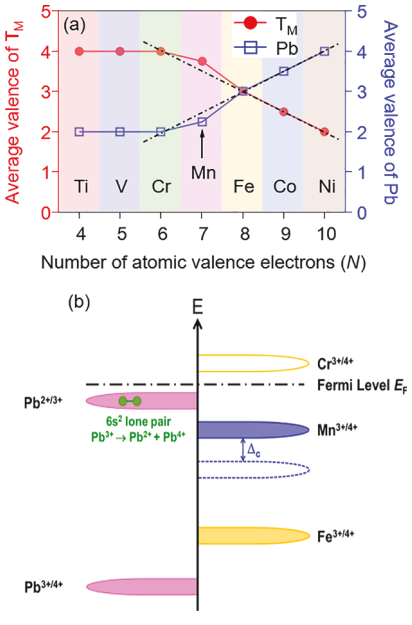

Figure 10. (a) Diagram of the average valence of Pb and transition metals T_M *vs* the number of atomic valence electrons of the transition metals in the whole PbT_MO_3 series and (b) schematic redox energy diagram representing various types of lead transition-metal perovskites.

It should be noted that in the cubic structure adding an electron to the e_g orbital on the Mn^{3+} cation would cost an extra energy Δ_c because of the crystal field splitting, which makes the $Mn^{3+/4+}$ redox level relatively higher than the $Fe^{3+/4+}$ redox but still lower than the $Pb^{2+/3+}$ redox. As a direct consequence, the population of electrons hopping from the $Pb^{2+/3+}$ redox to $Mn^{3+/4+}$ redox is essentially prohibited, which leads to the anomalous deviation of the valence state for $PbMnO_3$. Moreover, a calculation with SPuDS gives a $t = 1.01$ for $PbMnO_3$. A perovskite with a $t > 1$ would normally adopt a polar structure, especially with Pb^{2+} with the lone-pair electrons at the A-site, but a small percentage of Mn^{3+} corresponds to a partial occupation of the e_g orbital, which reduces the t factor of $PbMnO_3$ close to 1 or even less than 1. The separation of the two $6s^2$ lone-pair electrons on Pb is not energetically favored; therefore, the $Pb^{2+/3+}$ redox potential does not exist. The charge transfer between $Pb^{2+/3+}$ and $Mn^{3+/4+}$ always ends up with the charge disproportionation $2Pb^{3+} \rightarrow Pb^{2+} + Pb^{4+}$; whereas our result of XAS still gives a mixture of Pb^{2+} and Pb^{4+} cations in $PbMnO_3$, the SXRPD pattern does not show any signs of superlattice peaks, indicating a random distribution of Pb^{4+} in the matrix of Pb^{2+}.

4.3. Transport Properties. Although $PbMnO_3$ shows an activated temperature dependence of resistivity, it is still possible that electrons are itinerant in the oxide. Grain boundary scattering may be responsible for the activated $\rho(T)$ found in $PbMnO_3$. In the thermoelectric power measurement, however, the grain boundary effect makes no contribution to the result. The relatively low thermoelectric power at RT indicates a higher charge density than that seen in typical insulators. A large γ extracted from the specific heat measurement appears to support this argument. The most important evidence to support an itinerant electron behavior is from the Arrott plot of magnetization. In addition, a large ratio of μ_{eff} *versus* M_{sat} and a low T_c places $PbMnO_3$ at a location near $ZrZn_2$ in the Rhodes–Wohlfarth plot.[40]

4.4. Competing Magnetic Phases. The unusual isotherms at low magnetic fields for $T < T_c$ in the Arrott plot of Figure 6c attract our attention and a further analysis of these isotherms leads to an in-depth understanding of the magnetism of $PbMnO_3$. Let us start from the $M(H)$ loop at 1.8 K. The magnetization from the virgin state behaves like an AFM phase, as shown in Figure 11a. A field-induced magnetic transition to a FM phase onsets at a critical field H_{cm1} of 2700 Oe and terminates at ~3 T. This transition resembles a metamagnetism for itinerant electrons postulated by Wohlfarth and Rhodes.[41] Examples of metamagnetism have been reported in $Lu(Co_{0.94}Al_{0.06})_2$[42] (the inset in Figure 11a) and $ZrZn_2$ at a critical pressure where the ferromagnetism is suppressed.[43] If we leave out the wing from the virgin state (point A) to 9 T, the rest of the $M(H)$ loop, as shown in Figure 11b, exhibits a typical butterfly-shaped magnetization that has been observed in a molecular ferric wheel (MFW) $NaFe_6$[44] (the inset in Figure 11b). In the MFW $NaFe_6$, the

https://dx.doi.org/10.1021/acs.chemmater.0c02706
Chem. Mater. 2021, 33, 92−101

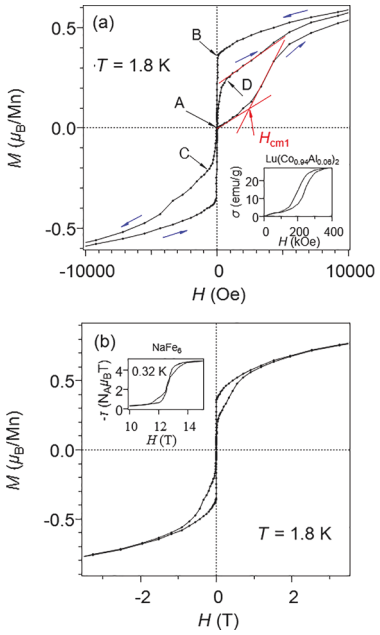

Figure 11. (a) Magnetization of $PbMnO_3$ at 1.8 K; the definition of critical field H_{cm1} for the metamagnetism transition is shown in the figure. The inset: magnetization of $Lu(Co_{0.94}Al_{0.06})_2$ (the data are after[42]) and (b) same as (a) without the wing from the virgin state. The inset: magnetization of the MFW $NaFe_6$ (the data are after[44]).

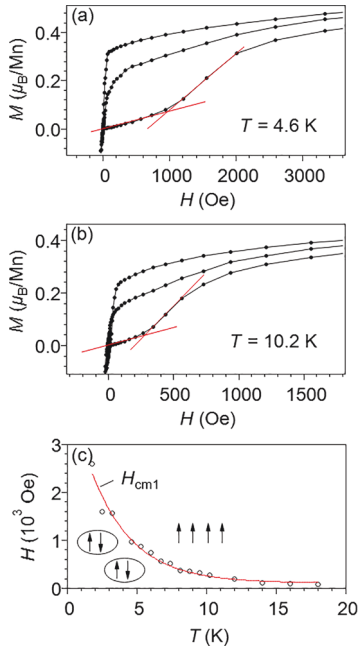

Figure 12. (a,b) Magnetization of $PbMnO_3$ at 4.6 and 10.2 K and (c) field-temperature magnetic phase diagram of $PbMnO_3$; the red line inside is the fitting result to a power law.

butterfly-shaped magnetization occurs at ∼ 12 T and 0.32 K. A strong field induces a spin-state change from $S = 0$ to $S = 1$. The heat associated with the spin-state change is channeled to the thermal bath *via* phonons, which are fewer at such a low temperature; the butterfly-shaped loop is formed owing to a phonon-bottleneck effect.[44] This effect is further confirmed by a scan-rate dependence of magnetization. The same physics can be applied to the magnetization of $PbMnO_3$. The only hypothesis we must make here is that there are two phases in $PbMnO_3$, that is, an AFM dimmer phase and a FM phase where the weak itinerant electron ferromagnetism is operative. The $M(H)$ loop found in Figure 11b is a combination of a loop because of the metamagnetic transition and a loop for a ferromagnet.

The abrupt drop of $M(H)$ at point B, as shown in Figure 11a, near the magnetic-field reversion distinguishes the butterfly-shaped loop of $PbMnO_3$ from the typical one in the literature. On top of the spin-state transition from "large" spin in the FM phase to "small" spin in the AFM dimmer phase, the magnetization reversal of the FM phase also occurs at this point. Because of the hysteresis associated with the high spin to low spin transition, a small percentage of the high spin phase persists at $H = 0$ on a part of the demagnetization loop from point B to point C and the moment in the residual high spin phase reverses. Point C and point D are symmetric; whereas the residual high-spin phase is nearly saturated at D, a further increase of the magnetic field is to magnetize the low spin phase. Therefore, the $M(H)$ curve is linear with increasing field from point D with the same slope of $M(H)$ from the virgin state (point A). An identical $M(H)$ loop can be found at all temperatures below 20 K; the $M(H)$ loops at 4.6 and 10.2 K are displayed in Figure 12a,b. These plots show that H_{cm1} lowers progressively as the temperature increases. The phase diagram showing the AFM phase and the FM phase is displayed in Figure 12c.

Owing to a charge transfer between Pb and Mn, the perovskite $PbMnO_3$ exhibits a complex magnetic property. As seen from the Arrott plot in Figure 6c, $PbMnO_3$ has the same exchange interaction at $T > 20$ K as in other itinerant electron ferromagnets. A competing AFM phase develops right below 20 K and gets strengthened as the temperature further decreases. It is highly unusual that a modest magnetic field can convert an AFM phase into a FM phase. The AFM phase appears to be responsible for the splitting between ZFC and FC curves, as shown in Figure 5a.

5. CONCLUSIONS

The perovskite $PbMnO_3$ offers a unique example that does not adopt either a polar structure or hexagonal polytype although its tolerance factor is slightly larger than 1. In addition, we have demonstrated the importance of global instability in addition to the t factor in order to synthesize the entire family of PbT_MO_3 perovskites. The crossover of two redox potentials of Pb and T_M, as Z of the 3d transition metal T_M increases, triggers a charge transfer between Pb and T_M in PbT_MO_3. In addition, a further oxidation of the lone-pair electrons on Pb induces a charge disproportionation $2Pb^{3+} \rightarrow Pb^{2+} + Pb^{4+}$. The new XAS results on $PbMnO_3$ allow us to fill the gap in the picture of the charge transfer and the charge disproportionation for the entire family of PbT_MO_3 perovskites.

Although an activated resistivity is observed, $PbMnO_3$ could become the only metallic oxide in the series of PbT_MO_3 as indicated by a large density-of-states at the Fermi energy extracted from the specific-heat measurement and a relatively small magnitude of thermoelectric power. Moreover, itinerant electron ferromagnetism in $PbMnO_3$ is supported by an observation of nearly linear isothermals in the Arrott plot of magnetization. Although a DFT calculation also predicts a FM metallic phase in PbMnO, there is a competing AFM phase below 20 K. The conversion from the AFM phase to a FM phase occurs at a modest magnetic field.

https://dx.doi.org/10.1021/acs.chemmater.0c02706
Chem. Mater. 2021, 33, 92−101

AUTHOR INFORMATION

Corresponding Author

Jianshi Zhou − *Materials Science and Engineering Program, Department of Mechanical Engineering, The University of Texas at Austin, Austin, Texas 78712, United States;* orcid.org/0000-0002-7667-5640; Email: jszhou@mail.utexas.edu

Authors

Xiang Li − *Key Laboratory of Advanced Optoelectronic Quantum Architecture and Measurement, Ministry of Education (MOE), School of Physics, Beijing Institute of Technology, Beijing 100081, China; Materials Science and Engineering Program, Department of Mechanical Engineering, The University of Texas at Austin, Austin, Texas 78712, United States;* orcid.org/0000-0003-4013-0259

Zhiwei Hu − *Max Planck Institute for Chemical Physics of Solids, Dresden 01187, Germany*

Yujin Cho − *Department of Physics, The University of Texas at Austin, Austin, Texas 78712, United States*

Xinyu Li − *Materials Science and Engineering Program, Department of Mechanical Engineering, The University of Texas at Austin, Austin, Texas 78712, United States*

Hao Sun − *Key Laboratory of Advanced Optoelectronic Quantum Architecture and Measurement, Ministry of Education (MOE), School of Physics, Beijing Institute of Technology, Beijing 100081, China*

Longzheng Cong − *Key Laboratory of Advanced Optoelectronic Quantum Architecture and Measurement, Ministry of Education (MOE), School of Physics, Beijing Institute of Technology, Beijing 100081, China*

Hong-Ji Lin − *National Synchrotron Radiation Research Center, Hsinchu 30076, Taiwan*

Sheng-Chieh Liao − *Max Planck Institute for Chemical Physics of Solids, Dresden 01187, Germany*

Chien-Te Chen − *National Synchrotron Radiation Research Center, Hsinchu 30076, Taiwan*

Anna Efimenko − *European Synchrotron Radiation Facility (ESRF), Grenoble 38000, France*

Christoph J. Sahle − *European Synchrotron Radiation Facility (ESRF), Grenoble 38000, France;* orcid.org/0000-0001-8645-3163

Youwen Long − *Beijng National Laboratory for Condensed Matter Physics, Institute of Physics, Chinese Academy of Sciences, Beijing 100190, China; Songshan Lake Materials Laboratory, Dongguan, Guangdong 523808, China;* orcid.org/0000-0002-8587-7818

Changqing Jin − *Beijng National Laboratory for Condensed Matter Physics, Institute of Physics, Chinese Academy of Sciences, Beijing 100190, China*

Michael C. Downer − *Department of Physics, The University of Texas at Austin, Austin, Texas 78712, United States*

John B. Goodenough − *Materials Science and Engineering Program, Department of Mechanical Engineering, The University of Texas at Austin, Austin, Texas 78712, United States;* orcid.org/0000-0001-9350-3034

Complete contact information is available at: https://pubs.acs.org/10.1021/acs.chemmater.0c02706

Author Contributions

J.Z. and X.L. conceived the idea and discussed with the other authors. X.L., Z.H., Y.C., X.Y.L, H.S., and L.C. performed the experiments. X.L. and J.Z. wrote the manuscript. All the authors analyzed the data and have given the approval to the final version of the manuscript.

Notes

The authors declare no competing financial interest.

ACKNOWLEDGMENTS

This work was supported in part by the National Natural Science Foundation of China (NSFC) grants 11904020, 11934017 and Beijing Institute of Technology Research Fund Program SKLEST QNKT20-03 in China and National Science Foundation grants DMR 1729588 and DMR 1905598 in USA. J.B.G. and M.C.D. were supported by Welch Foundation, Houston, Texas, in USA with grant numbers of F-1066 and F-1038. The ESRF is acknowledged for providing synchrotron radiation and C.H. is thanked for technical support during the XAS measurements at ID20. Z.H. acknowledges the support from the Max Planck-POSTECH-Hsinchu Center for Complex Phase Materials. Use of the APS at Argonne National Laboratory was supported by the U. S. Department of Energy, Office of Science, Office of Basic Energy Sciences, under contract no. DE-AC02-06CH11357.

REFERENCES

(1) Goodenough, J. B.; Zhou, J. Varied roles of Pb in transition-metal $PbMO_3$ perovskites (M= Ti, V, Cr, Mn, Fe, Ni, Ru). *Sci. Technol. Adv. Mater.* **2015**, *16*, 036003.

(2) Azuma, M.; Sakai, Y.; Nishikubo, T.; Mizumaki, M.; Watanuki, T.; Mizokawa, T.; Oka, K.; Hojo, H.; Naka, M. Systematic charge distribution changes in Bi-and Pb-3d transition metal perovskites. *Dalton Trans.* **2018**, *47*, 1371−1377.

(3) Chen, K.; Mijiti, Y.; Agrestini, S.; Liao, S.-C.; Li, X.; Zhou, J.; Di Cicco, A.; Baudelet, F.; Tjeng, L. H.; Hu, Z. Valence State of Pb in Transition Metal Perovskites $PbTMO_3$ (TM= Ti, Ni) Determined From X-Ray Absorption Near-Edge Spectroscopy. *Phys. Status Solidi B* **2018**, *255*, 1800014.

(4) Sakai, Y.; Yang, J.; Yu, R.; Hojo, H.; Yamada, I.; Miao, P.; Lee, S.; Torii, S.; Kamiyama, T.; Ležaić, M.; Bihlmayer, G.; Mizumaki, M.; Komiyama, J.; Mizokawa, T.; Yamamoto, H.; Nishikubo, T.; Hattori, Y.; Oka, K.; Yin, Y.; Dai, J.; Li, W.; Ueda, S.; Aimi, A.; Mori, D.; Inaguma, Y.; Hu, Z.; Uozumi, T.; Jin, C.; Long, Y.; Azuma, M. A-Site and B-Site Charge Orderings in an s−d Level Controlled Perovskite Oxide $PbCoO_3$. *J. Am. Chem. Soc.* **2017**, *139*, 4574−4581.

(5) Belik, A. A.; Azuma, M.; Saito, T.; Shimakawa, Y.; Takano, M. Crystallographic features and tetragonal phase stability of $PbVO_3$, a new member of $PbTiO_3$ family. *Chem. Mater.* **2005**, *17*, 269−273.

(6) Shpanchenko, R. V.; Chernaya, V. V.; Tsirlin, A. A.; Chizhov, P. S.; Sklovsky, D. E.; Antipov, E. V.; Khlybov, E. P.; Pomjakushin, V.; Balagurov, A. M.; Medvedeva, J. E.; Kaul, E. E.; Geibel, C. Synthesis, structure, and properties of new perovskite $PbVO_3$. *Chem. Mater.* **2004**, *16*, 3267−3273.

(7) Inaguma, Y.; Tanaka, K.; Tsuchiya, T.; Mori, D.; Katsumata, T.; Ohba, T.; Hiraki, K.-i.; Takahashi, T.; Saitoh, H. Synthesis, structural transformation, thermal stability, valence state, and magnetic and electronic properties of $PbNiO_3$ with perovskite-and $LiNbO_3$-type structures. *J. Am. Chem. Soc.* **2011**, *133*, 16920−16929.

(8) Cheng, J.; Kweon, K. E.; Larregola, S. A.; Ding, Y.; Shirako, Y.; Marshall, L. G.; Li, Z.-Y.; Li, X.; dos Santos, A. M.; Suchomel, M.; Matsubayashi, K.; Uwatoko, Y.; Hwang, G. S.; Goodenough, J. B.; Zhou, J.-S. Charge disproportionation and the pressure-induced insulator−metal transition in cubic perovskite $PbCrO_3$. *Proc. Natl. Acad. Sci. U.S.A.* **2015**, *112*, 1670−1674.

(9) Yu, R.; Hojo, H.; Watanuki, T.; Mizumaki, M.; Mizokawa, T.; Oka, K.; Kim, H.; Machida, A.; Sakaki, K.; Nakamura, Y.; Agui, A.; Mori, D.; Inaguma, Y.; Schlipf, M.; Rushchanskii, K. Z.; Ležaić, M.; Matsuda, M.; Ma, J.; Calder, S.; Isobe, M.; Ikuhara, Y.; Azuma, M. Melting of Pb charge glass and simultaneous Pb−Cr charge transfer in

$PbCrO_3$ as the origin of volume collapse. *J. Am. Chem. Soc.* **2015**, *137*, 12719−12728.
(10) Tsuchiya, T.; Saito, H.; Yoshida, M.; Katsumata, T.; Ohba, T.; Inaguma, Y.; Tsurui, T.; Shikano, M. High-Pressure Synthesis of a Novel $PbFeO_3$. *MRS Online Proc. Libr.* **2006**, *988*, 0988-QQ09-16.
(11) Oka, K.; Azuma, M.; Hirai, S.; Belik, A. A.; Kojitani, H.; Akaogi, M.; Takano, M.; Shimakawa, Y. Pressure-Induced transformation of 6H hexagonal to 3C perovskite structure in $PbMnO_3$. *Inorg. Chem.* **2009**, *48*, 2285−2288.
(12) Glazer, A. M.; Mabud, S. A. Powder profile refinement of lead zirconate titanate at several temperatures. II. Pure $PbTiO_3$. *Acta Crystallogr., Sect. B: Struct. Crystallogr. Cryst. Chem.* **1978**, *34*, 1065−1070.
(13) Goodenough, J. B.; Kafalas, J. A.; Longo, J. M. High-Pressure Synthesis. In *Preparative Methods in Solid State Chemistry*; Hagenmuller, P., Ed.; Academic Press, Inc: New York, London, 1972; pp 1−69.
(14) Bougerol, C.; Gorius, M. F.; Grey, I. E. $PbMnO_{2.75}$—a high-pressure phase having a new type of crystallographic shear structure derived from perovskite. *J. Solid State Chem.* **2002**, *169*, 131−138.
(15) Jin, C.-Q.; Zhou, J.-S.; Goodenough, J. B.; Liu, Q. Q.; Zhao, J. G.; Yang, L. X.; Yu, Y.; Yu, R. C.; Katsura, T.; Shatskiy, A.; Ito, E. High-pressure synthesis of the cubic perovskite $BaRuO_3$ and evolution of ferromagnetism in $ARuO_3$ (A= Ca, Sr, Ba) ruthenates. *Proc. Natl. Acad. Sci. U.S.A.* **2008**, *105*, 7115−7119.
(16) Cheng, J.-G.; Ishii, T.; Kojitani, H.; Matsubayashi, K.; Matsuo, A.; Li, X.; Shirako, Y.; Zhou, J.-S.; Goodenough, J.; Jin, C. High-pressure synthesis of the $BaIrO_3$ perovskite: A Pauli paramagnetic metal with a Fermi liquid ground state. *Phys. Rev. B: Condens. Matter Mater. Phys.* **2013**, *88*, 205114.
(17) Subramanian, S. S.; Natesan, B. Magnetic Ground State and Electronic Structure Calculations of $PbMnO_3$ using DFT. *Adv. Mater. Res.* **2014**, *895*, 420−423.
(18) Chmaissem, O.; Dabrowski, B.; Kolesnik, S.; Mais, J.; Brown, D.; Kruk, R.; Prior, P.; Pyles, B.; Jorgensen, J. Relationship between structural parameters and the Néel temperature in $Sr_{1-x}Ca_xMnO_3$ ($0< x < 1$) and $Sr_{1-y}Ba_yMnO_3$ ($y < 0.2$). *Phys. Rev. B: Condens. Matter Mater. Phys.* **2001**, *64*, 134412.
(19) Cheng, J.-G.; Zhou, J.-S.; Goodenough, J. Evolution of ferromagnetism in orthorhombic perovskites $Sr_{1-x}Pb_xRuO_3$. *Phys. Rev. B: Condens. Matter Mater. Phys.* **2010**, *81*, 134412.
(20) Rodriguez-Carvajal, J. FULLPROF: a program for Rietveld refinement and pattern matching analysis. *Satellite Meeting on Powder Diffraction of the XV Congress of the IUCr*: Toulouse, France:[sn], 1990.
(21) Sala, M. M.; Martel, K.; Henriquet, C.; Al Zein, A.; Simonelli, L.; Sahle, C. J.; Gonzalez, H.; Lagier, M.-C.; Ponchut, C.; Huotari, S.; Verbeni, R.; Krisch, M.; Monaco, G. A high-energy-resolution resonant inelastic X-ray scattering spectrometer at ID20 of the European Synchrotron Radiation Facility. *J. Synchrotron Radiat.* **2018**, *25*, 580−591.
(22) Blöchl, P. E. Projector augmented-wave method. *Phys. Rev. B: Condens. Matter Mater. Phys.* **1994**, *50*, 17953.
(23) Kresse, G.; Joubert, D. From ultrasoft pseudopotentials to the projector augmented-wave method. *Phys. Rev. B: Condens. Matter Mater. Phys.* **1999**, *59*, 1758.
(24) Kresse, G.; Hafner, J. Ab initio molecular-dynamics simulation of the liquid-metal−amorphous-semiconductor transition in germanium. *Phys. Rev. B: Condens. Matter Mater. Phys.* **1994**, *49*, 14251.
(25) Kresse, G.; Furthmüller, J. Efficient iterative schemes for ab initio total-energy calculations using a plane-wave basis set. *Phys. Rev. B: Condens. Matter Mater. Phys.* **1996**, *54*, 11169.
(26) Heyd, J.; Scuseria, G. E.; Ernzerhof, M. Hybrid functionals based on a screened Coulomb potential. *J. Chem. Phys.* **2003**, *118*, 8207−8215.
(27) Aimi, A.; Mori, D.; Hiraki, K.-i.; Takahashi, T.; Shan, Y. J.; Shirako, Y.; Zhou, J.; Inaguma, Y. High-Pressure Synthesis of A-Site Ordered Double Perovskite $CaMnTi_2O_6$ and Ferroelectricity Driven by Coupling of A-Site Ordering and the Second-Order Jahn−Teller Effect. *Chem. Mater.* **2014**, *26*, 2601−2608.
(28) Mitra, C.; Hu, Z.; Raychaudhuri, P.; Wirth, S.; Csiszar, S.; Hsieh, H.; Lin, H.-J.; Chen, C.; Tjeng, L. Direct observation of electron doping in $La_{0.7}Ce_{0.3}MnO_3$ using x-ray absorption spectroscopy. *Phys. Rev. B: Condens. Matter Mater. Phys.* **2003**, *67*, 092404.
(29) Vasiliev, A. N.; Volkova, O.; Lobanovskii, L.; Troyanchuk, I.; Hu, Z.; Tjeng, L.; Khomskii, D.; Lin, H.-J.; Chen, C.; Tristan, N. Valence states and metamagnetic phase transition in partially B-site-disordered perovskite $EuMn_{0.5}Co_{0.5}O_3$. *Phys. Rev. B: Condens. Matter Mater. Phys.* **2008**, *77*, 104442.
(30) Liang, G.; Liu, R. S.; Wang, L. V. XANES study of the valence of Pb in $(Tl_{0.5}Pb_{0.5})Sr_2Ca_{1-x}Y_xCu_2O_{7-\delta}$. *Int. J. Mod. Phys. B* **1999**, *13*, 3693−3696.
(31) Chen, C. T.; Sette, F.; Ma, Y.; Hybertsen, M. S.; Stechel, E. B.; Foulkes, W. M. C.; Schulter, M.; Cheong, S.-W.; Cooper, A. S.; Rupp, L. W., Jr.; Batlogg, B.; Soo, Y. L.; Ming, Z. H.; Krol, A.; Kao, Y. H. Electronic states in $La_{2-x}Sr_xCuO_{4+\delta}$ probed by soft-X-ray absorption. *Phys. Rev. Lett.* **1991**, *66*, 104.
(32) Varma, C. M. Missing valence states, diamagnetic insulators, and superconductors. *Phys. Rev. Lett.* **1988**, *61*, 2713.
(33) Savin, A.; Nesper, R.; Wengert, S.; Fässler, T. F. ELF: The electron localization function. *Angew. Chem., Int. Ed. Engl.* **1997**, *36*, 1808−1832.
(34) Zhou, J.-S.; Goodenough, J. Unusual evolution of the magnetic interactions versus structural distortions in $RMnO_3$ perovskites. *Phys. Rev. Lett.* **2006**, *96*, 247202.
(35) Palenik, G. J. Bond valence sums in coordination chemistry using oxidation state independent R-0 values. A simple method for calculating the oxidation state of manganese in complexes containing only Mn-O bonds. *Inorg. Chem.* **1997**, *36*, 4888−4890.
(36) Lufaso, M. W.; Woodward, P. M. Prediction of the crystal structures of perovskites using the software program SPuDS. *Acta Crystallogr., Sect. B: Struct. Sci.* **2001**, *57*, 725−738.
(37) Shahzad, K.; Khan, M. N.; Shabbir, G.; Bashir, J. Neutron and X-Ray diffraction crystal structure rietveld analysis of $PbTiO_3$ ceramics. *Ferroelectrics* **2011**, *414*, 155−161.
(38) Oka, K.; Yamada, I.; Azuma, M.; Takeshita, S.; Satoh, K. H.; Koda, A.; Kadono, R.; Takano, M.; Shimakawa, Y. Magnetic ground-state of perovskite $PbVO_3$ with large tetragonal distortion. *Inorg. Chem.* **2008**, *47*, 7355−7359.
(39) Arévalo-López, Á. M.; Dos santos-García, A. J.; Alario-Franco, M. Á. Antiferromagnetism and spin reorientation in "$PbCrO_3$". *Inorg. Chem.* **2009**, *48*, 5434−5438.
(40) Wohlfarth, E. P. Very Weak Itinerant Ferromagnets - Application to ZrZn2. *J. Appl. Phys.* **1968**, *39*, 1061.
(41) Wohlfarth, E. P.; Rhodes, P. Collective Electron Metamagnetism. *Philos. Mag.* **1962**, *7*, 1817.
(42) Iijima, M.; Endo, K.; Sakakibara, T. Metamagnetism of itinerant d-electrons in Laves phase compounds $Lu(Co_{1-x}Al_x)_2$. *J. Phys.: Condens. Matter* **1990**, *2*, 10069.
(43) Uhlarz, M.; Pfleiderer, C.; Hayden, S. Quantum Phase Transitions in the Itinerant Ferromagnet $ZrZn_2$. *Phys. Rev. Lett.* **2004**, *93*, 256404.
(44) Waldmann, O.; Koch, R.; Schromm, S.; Müller, P.; Bernt, I.; Saalfrank, R. Butterfly hysteresis loop at nonzero bias field in antiferromagnetic molecular rings: cooling by adiabatic magnetization. *Phys. Rev. Lett.* **2002**, *89*, 246401.

https://dx.doi.org/10.1021/acs.chemmater.0c02706
Chem. Mater. 2021, 33, 92−101